Discovery of moganite in a lunar meteorite as a trace of H2O ice in the Moon's regolith

AUTHOR(S):

Kayama, Masahiro; Tomioka, Naotaka; Ohtani, Eiji; Seto, Yusuke; Nagaoka, Hiroshi; Götze, Jens; Miyake, Akira; ... Shoda, Naoki; Hirao, Naohisa; Kobayashi, Takamichi

CITATION:

Kayama, Masahiro ...[et al]. Discovery of moganite in a lunar meteorite as a trace of H2O ice in the Moon's regolith. Science Advances 2018, 4(5): eaar4378.

ISSUE DATE:

2018-05-02

URL:

http://hdl.handle.net/2433/231031

PLANETARY SCIENCE

Discovery of moganite in a lunar meteorite as a trace of H_2O ice in the Moon's regolith

Masahiro Kayama,[1,2]* Naotaka Tomioka,[3] Eiji Ohtani,[1] Yusuke Seto,[4] Hiroshi Nagaoka,[5] Jens Götze,[6] Akira Miyake,[7] Shin Ozawa,[1] Toshimori Sekine,[8,9] Masaaki Miyahara,[8] Kazushige Tomeoka,[4] Megumi Matsumoto,[4] Naoki Shoda,[4] Naohisa Hirao,[10] Takamichi Kobayashi[11]

Moganite, a monoclinic SiO_2 phase, has been discovered in a lunar meteorite. Silica micrograins occur as nanocrystalline aggregates of mostly moganite and occasionally coesite and stishovite in the KREEP (high potassium, rare-earth element, and phosphorus)–like gabbroic-basaltic breccia NWA 2727, although these grains are seemingly absent in other lunar meteorites. We interpret the origin of these grains as follows: alkaline water delivery to the Moon via carbonaceous chondrite collisions, fluid capture during impact-induced brecciation, moganite precipitation from the captured H_2O at pH 9.5 to 10.5 and 363 to 399 K on the sunlit surface, and meteorite launch from the Moon caused by an impact at 8 to 22 GPa and >673 K. On the subsurface, this captured H_2O may still remain as ice at estimated bulk content of >0.6 weight %. This indicates the possibility of the presence of abundant available water resources underneath local sites of the host bodies within the Procellarum KREEP and South Pole Aitken terranes.

INTRODUCTION

Various water species (for example, H_2O ice, OH bound to minerals, and hydrated phases) have been detected at local sites of the high-latitude lunar surface by remote sensing spacecraft (*1*, *2*). H_2O ice is concentrated locally near the poles as a result of horizontal molecular migration from the sunlit surface at lower latitudes toward the higher latitudes along the temperature gradient between the equator and the poles; H^+ and OH^- species photodissociated from H_2O are subsequently cold-trapped in the permanently shadowed regions (PSRs) (*1*, *3*). This solar photodissociation process also leads to the vertical migration of H_2O molecules on the sunlit surface to the entire Moon's subsurface (*3*, *4*). Consequently, H_2O molecules could theoretically accumulate as ice in the lower-temperature subsurface regolith at roughly a few hundred parts per million (ppm) at depths ranging from 10^{-4} to more than 10^2 m (*3*). Only sparse evidence for H_2O beneath the top few millimeters of the regolith exists (*2*) because neutron spectrometers cannot distinguish forms of H and near-infrared spectrometers are only sensitive to the optical surface of the regolith (*5*). Furthermore, traces of H_2O ice have not yet been reported from the Apollo or Luna rocks or from lunar meteorites. Therefore, uncertainties remain regarding the nature and amount of H_2O ice in the Moon's subsurface.

Here, we investigated 13 different lunar meteorites with various lithologies (gabbro, basalt, anorthositic regolith, troctolite, and their breccias) using micro-Raman spectrometry, electron microscopy, and synchrotron angle-dispersive x-ray diffraction (SR-XRD) (see Materials and Methods). We discovered moganite, a monoclinic SiO_2 phase (*6*–*8*), coexisting with coesite and stishovite only in the KREEP (high potassium, rare-earth element, and phosphorus)–like gabbroic-basaltic brecciated meteorite NWA 2727. Our findings demonstrate that moganite in NWA 2727 is most likely to have been formed during lunar fluid activity on the sunlit surface and that the source fluid was probably cold-trapped as H_2O ice in the subsurface. We also present a possible formation process for lunar moganite and evaluate the bulk content, pH, distribution, and origin of the Moon's subsurface H_2O.

RESULTS

Silica in lunar meteorites

NWA 2727 is found to be mainly composed of olivine-cumulate (OC) gabbroic and basaltic clasts containing a breccia matrix (Fig. 1) (see also Materials and Methods), where the breccia matrix and basaltic clasts contain several silica varieties. Silica occurs as amygdaloidal anhedral micrograins (2 to 13 μm in radius) between the constituent minerals of the breccia matrix (fig. S1, A and B). The Raman spectra of many silica micrograins (n = 102) in the breccia matrix show characteristics of moganite (Figs. 2 and 3) (*6*–*8*). Quartz Raman bands are also found in other parts, but coesite bands are identified together with the moganite signature at the boundaries of these micrograins. The Raman spectra of these micrograins could be deconvolved into moganite, coesite, and quartz components centered at 502, 521, and 464 cm^{-1}, respectively (see Materials and Methods). As a result of combining their intensity ratios with the calibration curve (*8*, *9*), the moganite contents [that is, weight % (wt %) against the other SiO_2 polymorphs (*6*–*9*)] of the breccia matrix–hosted silica micrograins are inferred to be 37 to 96 wt % with an average of 77 wt %. The Raman intensity maps of these micrograins demonstrate that moganite (502 cm^{-1}) coexists with coesite (521 cm^{-1}), although the abundance of quartz (464 cm^{-1}) is negatively correlated with those of moganite and coesite. Moganite is obviously enriched in the cores but is depleted or almost absent in the rims. Furthermore, the silica micrograins contain abundant coesite at their boundaries rather than in the cores.

In the continuous shock veins crosscutting the breccia matrix of NWA 2727 (fig. S2) (see Materials and Methods), we discovered amygdaloidal

[1]Department of Earth and Planetary Materials Science, Graduate School of Science, Tohoku University, Sendai 980-8578, Japan. [2]Creative Interdisciplinary Research Division, Frontier Research Institute for Interdisciplinary Sciences, Tohoku University, Sendai 980-8578, Japan. [3]Kochi Institute for Core Sample Research, Japan Agency for Marine-Earth Science and Technology, 200 Monobe Otsu, Nankoku, Kochi 783-8502, Japan. [4]Department of Planetology, Graduate School of Science, Kobe University, 1-1 Rokkodai-cho, Nada-ku, Kobe 657-8501, Japan. [5]Research Institute for Science and Engineering, Waseda University, Shinjuku, Tokyo 169-8555, Japan. [6]TU Bergakademie Freiberg, Institute of Mineralogy, Brennhausgasse 14, 09596 Freiberg, Germany. [7]Department of Geology and Mineralogy, Graduate School of Science, Kyoto University, Kitashirakawa-Oiwake, Sakyo-ku, Kyoto 606-8502, Japan. [8]Department of Earth and Planetary Systems Science, Graduate School of Science, Hiroshima University, Higashi-Hiroshima 739-8526, Japan. [9]Center for High Pressure Science and Technology Advanced Research, Pudong, Shanghai 201203, P.R. China. [10]Japan Synchrotron Radiation Research Institute, 1-1-1 Kouto Sayo, Hyogo 679-5198, Japan. [11]National Institute for Materials Science, 1-1 Namiki, Tsukuba, Ibaraki 305-0044, Japan.
*Corresponding author. Email: kayama0127@gmail.com

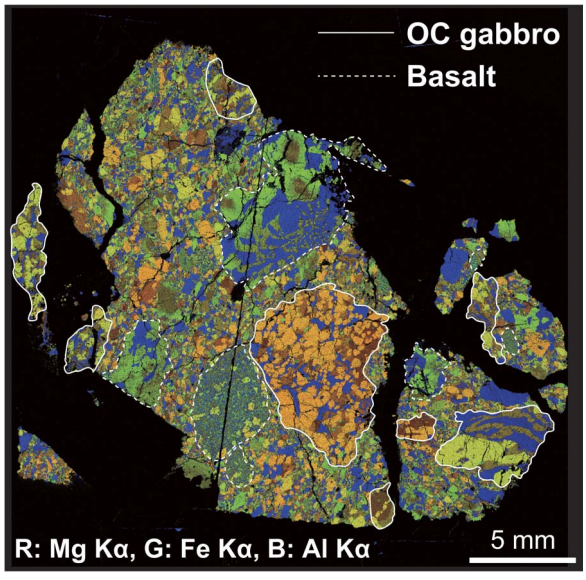

Fig. 1. Petrological photographs of NWA 2727. False-color elemental x-ray map of the NWA 2727 thin section, with red (R) = Mg Kα, green (G) = Fe Kα, and blue (B) = Al Kα x-rays obtained by the electron probe microanalyzer (EPMA). Areas enclosed by white lines indicate Mg/Fe-rich OC gabbroic clasts, including abundant coarse grains of euhedral olivine (orange and yellow) and clinopyroxene (brown and green) accompanied by minor amounts of anhedral plagioclase (blue) between these constituent minerals. The pyroxene phyric basaltic clasts (highlighted by dashed white lines) are characterized by clinopyroxene phenocrysts with a fine-grained groundmass of clinopyroxene, plagioclase, and fine quartz grains. The other areas filling the interstices between these clasts represent the breccia matrix composed of numerous fine to coarse grains of the OC gabbro and basalt lithic minerals with small amygdaloidal silica micrograins.

silica micrograins (n = 4) with a tweed-like rim texture, surrounded by olivine, clinopyroxene, plagioclase, and their glasses, with bubble and flow marks (fig. S1, C and D). The Raman spectra of the tweed-textured rim characteristically consist of pronounced peaks of coesite and weak bands corresponding to stishovite (Fig. 4). Raman bands corresponding to moganite (*6*–*8*) and shock-induced silica glass (*10*) are identified in the grain cores. The Raman intensity maps of this silica micrograin also reveal the presence of coesite (521 cm^{-1}) and stishovite (753 cm^{-1}) in the rim, whereas moganite (502 cm^{-1}) and shock-induced silica glass (602 cm^{-1}) are abundant in the cores. A Raman spectral pattern corresponding to cristobalite is also detected in other silica micrograins entrained in the shock veins, together with coesite and moganite signatures (fig. S3). Raman intensity mapping reveals the presence of cristobalite (416 cm^{-1}) and moganite (502 cm^{-1}) abundantly distributed in the cores, whereas coesite (521 cm^{-1}) is identified in the rims of these silica micrograins. The moganite content of these silica micrograins within shock veins ranges from 6 to 46 wt % with an average of 24 wt %. This value is considerably lower than those of the breccia matrix–hosted silica micrograins far from the shock veins (37 to 96 wt % with an average of 77 wt %).

On the basis of the micro-Raman spectrometry and electron microscopy results for NWA 2727, coarse grains of euhedral tridymite and cristobalite (20 to 100 μm in radius; n = 35) are also observed (fig. S4A), although no signals of moganite, coesite, or stishovite are detected. Small single crystals of anhedral quartz (10 to 20 μm in radius; n = 23) are present in the basaltic clasts, although they do not coexist with other silica polymorphs (figs. S4B and S5). The OC gabbroic clasts of NWA 2727 and the paired lunar meteorites of nonbrecciated OC gabbroic NWA 2977, 3333, and 6950 [that is, the NWA 773 clan (*11*, *12*); see Materials and Methods] contain no silica at all. In addition, we identified silica crystals in some of the remaining lunar meteorites selected here (see Materials and Methods), although moganite is not found, except for in the breccia matrix of NWA 2727.

The Raman and cathodoluminescence (CL) spectroscopy data from within the shock veins of NWA 2727 display the characteristic spectral patterns of maskelynite, whereas the signatures of crystalline plagioclase are detected in both the breccia matrix and the clasts located far from the shock veins (fig. S6).

Identification and observation of moganite and high-pressure SiO_2 phases

Several of these amygdaloidal silica micrograins were extracted as square cubic blocks (about 10 μm per side) with a focused ion beam (FIB) system for SR-XRD analysis (see Materials and Methods). The SR-XRD patterns of the extracted square cube portions from the silica micrograins of the breccia matrix of NWA 2727 show strong peaks at d values of 4.46 and 3.36 Å and weak peaks at 2.31, 2.19, 2.04, 1.97, 1.83, and 1.66 Å (fig. S7A). These diffractions can be indexed to a monoclinic lattice with the following cell parameters: a = 8.77(1) Å, b = 4.90(1) Å, c = 10.77(3) Å, β = 90.38(3)°, and V = 463.0(6) Å as the space group $I2/a$, in good agreement with the structure of moganite. The diffraction lines of the cubes from the silica micrograins entrained in the shock veins are observed at d values of 2.97, 2.26, 2.10, 1.99, and 1.88 Å (fig. S7B). The calculated unit-cell parameters [a = 4.19(9) Å, c = 2.68(1) Å, and V = 47.3(1) Å, as the space group $P4_2/mnm$] correspond well to those of stishovite. The reflections of both cubes at d values of 6.22, 4.40, 3.45, 3.12, 2.78, 2.71, 1.80, 1.73, and 1.66 Å (fig. S7, A and B) can also be indexed to a monoclinic unit cell (space group = $C2/c$) with a = 7.14(1) Å, b = 12.45(8) Å, c = 7.17(7) Å, β = 120.02(2)°, and V = 552.8(4) Å. It can be identified as coesite. Apart from these cubes, excavated blocks from other silica micrograins within the shock veins exhibit an SR-XRD pattern with weak lines at d = 4.10, 2.89, 2.16, and 1.71 Å together with the characteristic reflections of moganite (fig. S7C). The d values are in good agreement with those of cristobalite. Thus, the silica micrograins containing moganite are recognized only in the breccia matrix far from and within the shock veins, although they are not observed in the gabbroic and basaltic clasts of NWA 2727. Anhedral fine-grained quartz in the basaltic clasts and euhedral coarse-grained tridymite and cristobalite of NWA 2727 (fig. S4) also show no moganite signatures. Moreover, we did not discover moganite in the other lunar meteorites selected here.

These cubic blocks of the silica micrograins were sliced (<100 nm thickness) by FIB for transmission electron microscopy (TEM) observations. Annular dark-field scanning TEM (STEM) images and false-color elemental maps of these sliced thin-foil samples reveal the presence of large SiO_2 regions (1.5 to 3.0 μm in radius) in contact with small clinopyroxene, olivine, and plagioclase regions (0.5 to 1.0 μm in radius) (fig. S8). According to the bright-field TEM imaging results of the FIB-sliced silica micrograins from the breccia matrix, the SiO_2 regions consist of nanocrystalline aggregates of numerous euhedral or subhedral silica particles with an average radius of 4.5 nm (radii of 2.6 to 107.6 nm for n = 148) (Fig. 5, A and B). Most of the selected area electron diffraction (SAED) patterns (spot size, 60 nm in radius) of the nanometer-scale silica particles coincide with that of moganite. Thus, a set of SAED profiles taken from the largest of these grains (107.6 nm in radius) with an angular relationship of 25.2° is consistent with the structure

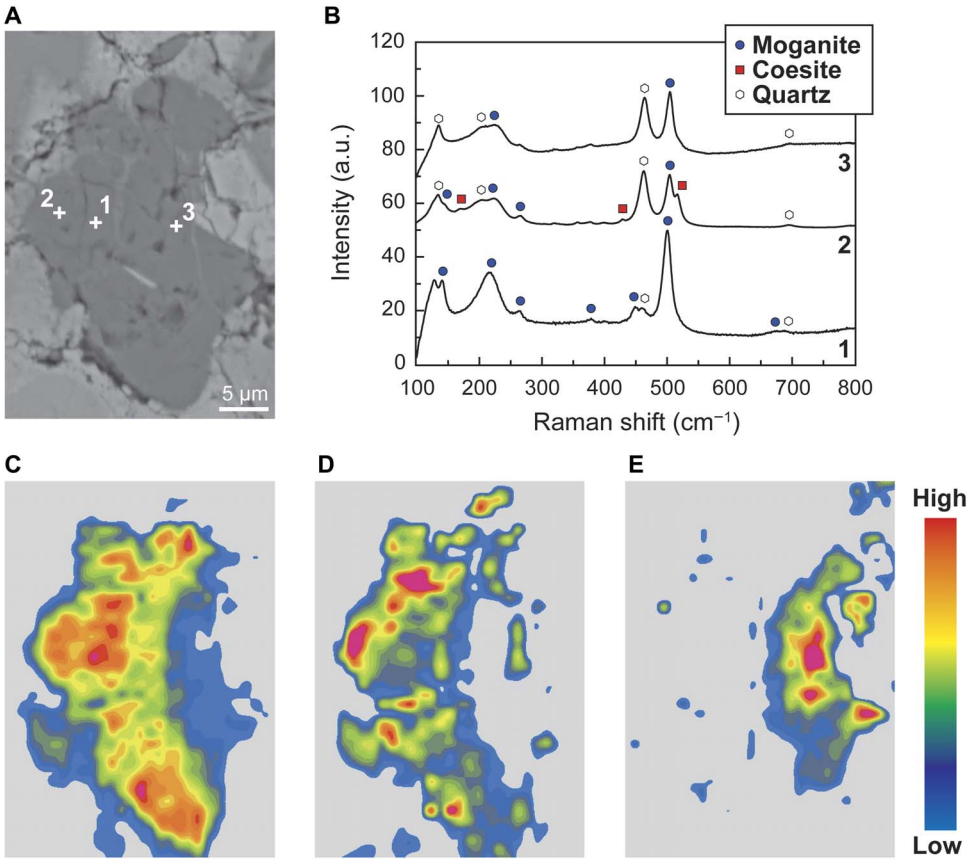

Fig. 2. Micro-Raman spectroscopy and mapping of an amygdaloidal silica micrograin in the breccia matrix. (**A**) High-magnification BSE image of an amygdaloidal silica micrograin (no. 1) in the breccia matrix of NWA 2727. White crosses indicate the analytical points for Raman spectroscopy (areas 1 to 3). (**B**) Raman spectra of areas 1 to 3 of the silica micrograin in (A) showing a negative correlation between the Raman intensities of the moganite and the quartz bands. Obvious coesite bands are present together with the moganite signature in the rim of the silica micrograin (area 2). a.u., arbitrary units. (**C** to **E**) Raman intensity maps of the moganite (502 cm^{-1}) (C), coesite 21 cm^{-1}) (D), and quartz (464 cm^{-1}) (E) bands for the silica micrograin. Red and blue denote the high- and low-relative Raman intensities of each silica band, respectively. Moganite becomes dominant at the left part of the silica micrograin, whereas quartz is abundant in the right part. Coesite coexists with moganite and occurs in the outermost rim of the left, as indicated by the areas of overlap in the spectra.

of moganite along the [001] and [$0\bar{1}1$] zone axes (Fig. 5, B to D). Furthermore, the SAED profiles of moganite were obtained from both this largest grain and the aggregates of numerous fine nanoparticles (average radius of 4.5 nm). We also identified several SiO_2 nanoparticles of subhedral coesite in the FIB-sliced silica micrograins in both the breccia matrix and the shock veins (fig. S9, A and D). Columnar stishovite and anhedral cristobalite phases are identified from TEM observations of the silica micrograins entrained in the shock veins (fig. S9, B, C, E, and F). Thus, abundant moganite is accompanied by small amounts of coesite in all cases, whereas stishovite and cristobalite are present together with moganite only in the silica micrograins within the shock veins. Our SR-XRD and TEM investigations confirm the presence of moganite in the breccia matrix of NWA 2727, but we have not identified it in the other lithologies or lunar meteorites we examined.

DISCUSSION

Origin of moganite in NWA 2727

Moganite is a metastable phase of monoclinic SiO_2 that belongs to the *I*2/*a* space group (*6*). On Earth, it has been shown that moganite contents of 5 to 100 wt % form through precipitation of nano- to microcrystalline SiO_2 from alkaline fluids only in sedimentary settings (that is, under high consolidation pressure) (*6*–*8*, *13*–*17*). Thermochemically unstable moganite readily transforms into quartz or dissolves during silica-water interactions at ambient pressure, resulting in moganite-free phases in altered rocks exposed to weathering processes (*13*–*16*, *18*). For instance, the weathered surfaces of microcrystalline silica grains consistently contain less moganite than the pristine interiors (*6*, *7*, *13*). Moreover, no terrestrial rocks with moganite older than 130 million years (Ma) ago have been found because its thermochemical instability causes the moganite content to decrease with age (*6*–*8*, *13*–*16*). On the basis of laboratory hydrothermal experiments, moganite has been synthesized via high pressure–induced polycondensation (about >100 MPa) and dehydroxylation of colloidal silicic acid upon changes in pH from 9.5 to 12.0 to 13.0 at 373 to 418 K (*17*, *18*). Molecular dynamics simulations of SiO_2 phases (*19*) have also demonstrated that moganite has an orthorhombic symmetry (space group *Ibam*) at ambient pressure, whereas monoclinic moganite (*I*2/*a*) in a naturally occurring form is stable in the pressure range from 6 to 21 GPa at 300 K. According to these previous investigations, on Earth, some monoclinic moganite has been preserved at concentrations from 5 to 100 wt % in unaltered and

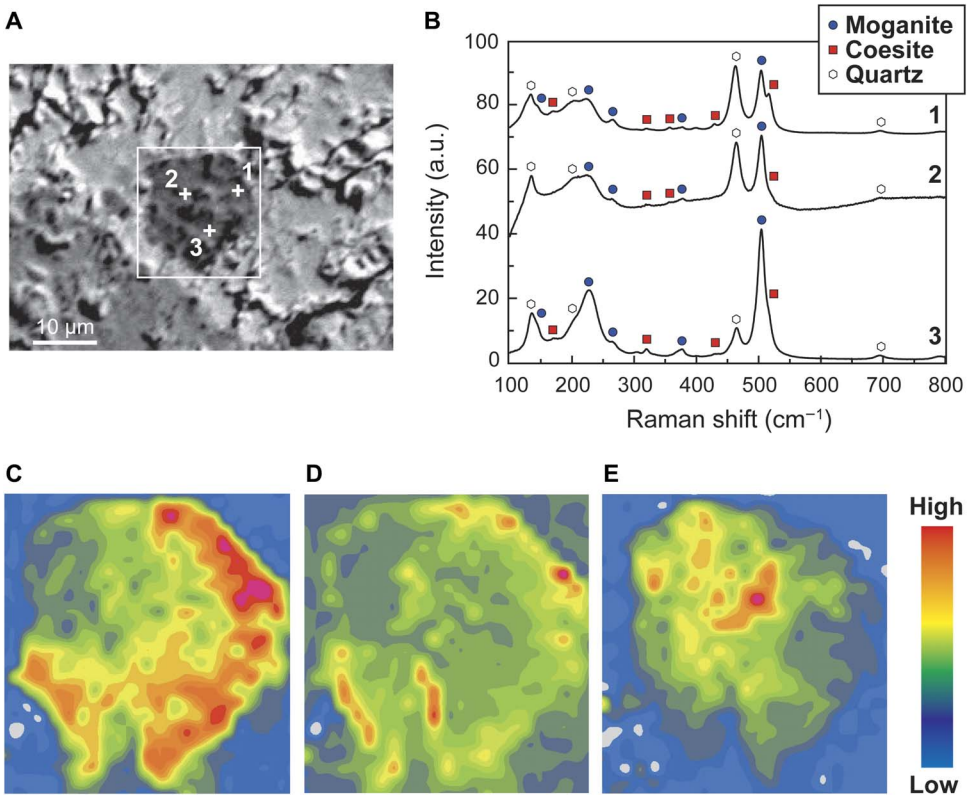

Fig. 3. Micro-Raman analyses of another amygdaloidal silica micrograin in the breccia matrix. (**A**) High-magnification BSE image of another amygdaloidal silica micrograin (no. 2) in the breccia matrix of NWA 2727 far from the shock veins. White crosses and white boxes indicate the analytical points of Raman spectroscopy (areas 1 to 3) and the mapping areas, respectively. (**B**) Raman spectra of the different areas of the silica micrograin in (A). Raman intensities of the moganite bands increase, whereas those of the quartz bands decrease. The most intense coesite bands are detected together with moganite signatures in the rim of the silica micrograin (area 1). (**C** to **E**) Raman intensity maps of the moganite (502 cm^{-1}) (C), coesite (521 cm^{-1}) (D), and quartz (464 cm^{-1}) (E) bands for the silica micrograin. Red and blue denote the high- and low-relative Raman intensities of each silica band, respectively. Moganite is abundant in the right and lower left of the silica micrograin, being present with coesite in the outermost rim of these parts. In contrast, quartz is located in the upper left, and its distribution is opposite to those of moganite and coesite.

consolidated sedimentary rocks (for example, evaporite, chert, and cavities in sedimentary breccia) younger than 130 Ma old (that is, no burial), and it is apparently absent in terrestrially weathered specimens (*6*–*8*, *13*–*18*).

These mineralogical descriptions and laboratory experiments (*6*–*8*, *13*–*18*) imply that moganite (37 to 96 wt % with an average of 77 wt %) in NWA 2727 is highly likely to have been precipitated from high-pressure alkaline fluid activity on the Moon, rather than being formed under ambient terrestrial weathering conditions in the hot desert where the meteorites were found. In addition, moganite is exclusively distributed in the breccia matrix of NWA 2727, whereas it is absent from the remaining lithologies and other lunar meteorites. No moganite signatures were detected by the microanalyses performed here on fine-grained quartz present in the basaltic clasts and coarse-grained tridymite and cristobalite in NWA 2727 (fig. S4), not even in the grain rims that would have been most significantly affected by terrestrial weathering. The possibility that the moganite in NWA 2727 was transformed from unhydrated silica minerals (for example, quartz, tridymite, and cristobalite) is ruled out by these observations, even if silica-water interaction occurred during terrestrial weathering, as indicated by previous work (*17*, *18*). Only a few hot desert meteorites contain weathering products of vein-filling silica coexisting with hydrous minerals (jarosite and dissolved olivine/pyroxene) (*20*). However, our SR-XRD and TEM examinations indicate that these hydrous minerals are absent in olivine, pyroxene, and plagioclase in contact with and far from the silica varieties of NWA 2727. Furthermore, our scanning electron microscopy (SEM) observations reveal the presence of Fe-Ni metals in the breccia matrix, which implies that less terrestrial weathering affected NWA 2727, at least in terms of nonterrestrial formation of silica (*21*). The gabbroic clasts of NWA 2727 and the paired lunar meteorites of nonbrecciated gabbroic NWA 2977, 3333, and 6950 include neither moganite nor other silica polymorphs, despite having the same terrestrial ages and the same fall locations in a hot desert (that is, exactly the same extent of terrestrial weathering for all NWA 773 clan members) (*11*, *12*, *22*). That is, the silica varieties found in NWA 2727 (figs. S1 and S4) should also be present in the gabbroic lithologies of NWA 2727 and the paired lunar meteorites NWA 2977, 3333, and 6950, if they were produced by such terrestrial weathering, but this scenario was not the case. These facts also demonstrate that moganite does not form without brecciation under high consolidation pressure, as indicated in previous works (*6*–*8*, *13*–*19*). Furthermore, moganite is not observed in other lithic lunar meteorites (NWA 032, 4734, 5000, 5744, 6355, 8599, 8668, and 10649 and Dar al Gani 400), which indicates that its existence is a unique characteristic of the gabbroic-basaltic breccia matrix of NWA 2727. These findings suggest that the moganite-bearing silica micrograins precipitated from lunar alkaline fluids during high-pressure consolidation via impact-induced brecciation of the host gabbroic-basaltic bodies, that is, a local site of the birthplace of NWA 2727.

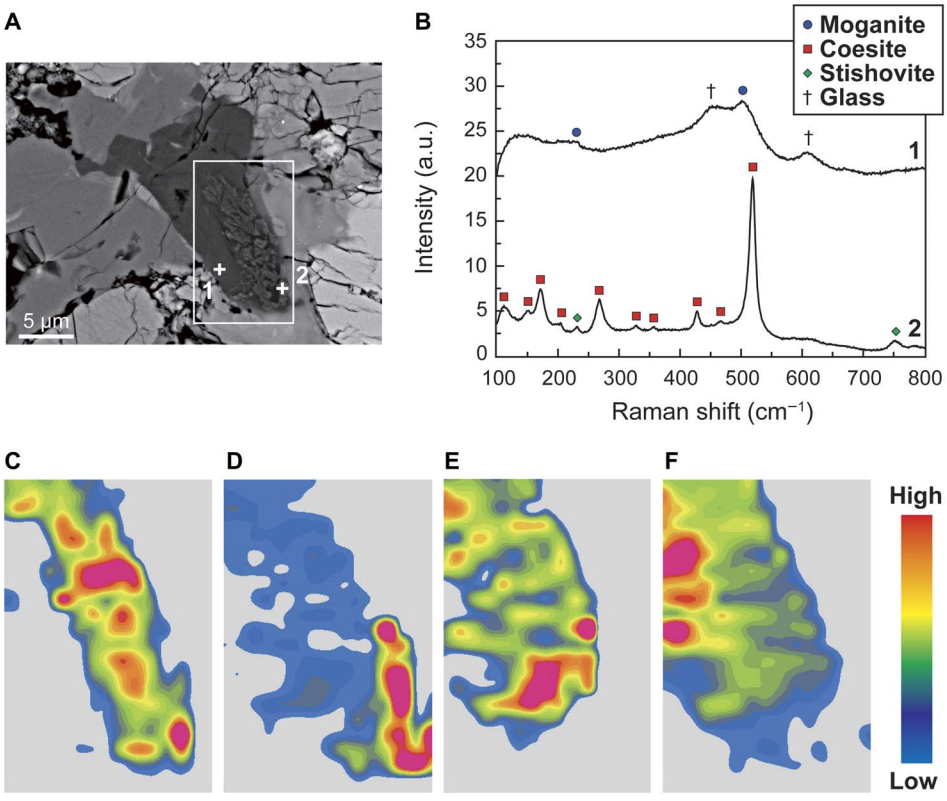

Fig. 4. Micro-Raman analyses of high-pressure SiO_2 phases. (**A**) High-magnification BSE image of an amygdaloidal silica micrograin (no. 3) within a shock vein. Tweed-like textures occur in the rim of this micrograin (lower right). White crosses and white boxes indicate the analytical points for Raman spectroscopy (areas 1 and 2) and the mapping areas, respectively. (**B**) Raman spectra of the silica micrograin in areas with and without the tweed-like textures. Only moganite and high-pressure silica glass signatures are detected in the area without the tweed-like textures (area 1). In contrast, stishovite and coesite signals become dominant in the tweed-textured rim (area 2). (**C** to **F**) Raman intensity maps of the stishovite (753 cm^{-1}) (C), coesite (521 cm^{-1}) (D), moganite (502 cm^{-1}) (E), and shock-induced silica glass (602 cm^{-1}) (F) bands. The relative Raman intensities are represented by color variations from red (high) to blue (low). Abundant stishovite coexists with coesite in the tweed-like textural rim (lower right). In contrast, moganite and shock-induced silica glass are quite depleted in the rim and enriched in the interior without the tweed-like texture.

Additional important evidence is that moganite is invariably found to coexist with coesite and/or stishovite within each silica micrograin (n = 102) in the breccia matrix of NWA 2727. These high-pressure SiO_2 phases mixed with moganite as nanocrystalline silica aggregates cannot form via terrestrial weathering. According to previous studies (*23*), low-pressure SiO_2 phases (that is, α-tridymite and α-cristobalite) are present with coesite and/or stishovite as nanocrystalline aggregates inside single silica grains in lunar and Martian meteorites found in the same hot desert as NWA 2727. Thus, some of these phases were transformed by solid-state reactions into these high-pressure SiO_2 phases within a closed system of grains via impact events on their parent bodies (*23*). This interpretation is further supported by the suggestion that the high-pressure SiO_2 phases in these meteorites formed at a shock temperature below the melting point (*10*, *23*). Similarly, in the case of NWA 2727, moganite is thought to be a precursor of coesite and stishovite, rather than the other silica polymorphs, because only moganite coexists with these high-pressure SiO_2 phases in the grain. In addition, the silica micrograins containing moganite are characterized by shock-induced textures of pervasive radiating cracks (figs. S1 and S4), as reported for shocked meteorites (*23*).

Within almost all the silica micrograins, moganite-rich domains are located inside coesite and stishovite outer rims (Figs. 2 to 4 and fig. S3). These findings can be explained by the fact that impact-induced compaction in meteorites generates significantly higher shock pressure and temperature at the grain boundaries compared with the interior (*24*). Therefore, speculation about moganite formation as a result of terrestrial weathering after fall can be excluded, because this scenario would result in the opposite texture, that is, a more strongly weathered rim dominated by moganite and a core rich in high-pressure SiO_2 phases and poor in moganite.

Furthermore, coesite and stishovite are accompanied by moganite, although these silica polymorphs are quite depleted in quartz-rich domains (Figs. 2 to 4 and fig. S3). The high-pressure SiO_2 phases are also absent from the fine-grained quartz and coarse-grained tridymite and cristobalite phases (figs. S4 and S5). Thus, these observations imply that the coesite and stishovite discovered in NWA 2727 were not produced by phase transitions from these silica varieties except for moganite. Solid-state phase transition of moganite to coesite occurs more readily than solid-state phase transitions of other silica varieties such as quartz, tridymite, and cristobalite because of its significantly lower kinetic barrier (*18*, *19*, *25*). This low kinetic barrier can be explained by the following two factors: the structural similarity of moganite and coesite and the presence of available water. Among silica polymorphs, only coesite and moganite structures are dominated by four-member rings of SiO_4 tetrahedra (*6*, *7*, *13*, *18*, *19*). According to high-pressure experimental results for silica (*19*, *25*), common four-member SiO_4 rings tend to reduce the kinetic barrier for the transition of moganite to coesite because this reaction energetically minimizes the reconstruction of Si–O bonds. This

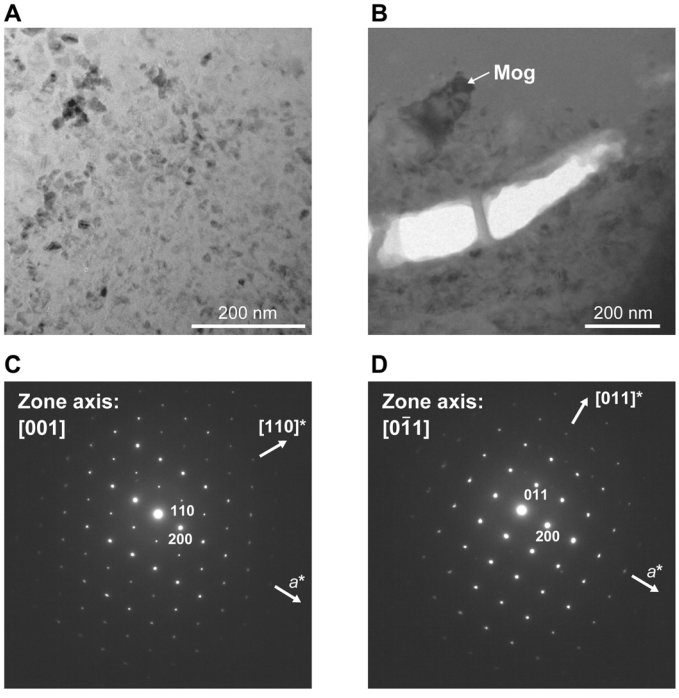

Fig. 5. TEM observation of moganite. (**A** and **B**) Bright-field TEM images of nanocrystalline aggregates (A) and the largest grain (107.6 nm in radius) (B) of moganite (Mog) taken from the SiO_2 region of the silica micrograin (no. 1) (red in fig. S8A). (**C** and **D**) SAED patterns of moganite along the [001] (C) and [0$\bar{1}$1] (D) zone axes. The diffraction patterns were acquired from the same largest grain within the SiO_2 region, with an angular relationship of 25.2° between them. Both the aggregates of numerous fine nanoparticles (average radius of 4.5 nm) and the largest grain show spot diffraction patterns corresponding to a moganite structure rather than Debye-Scherrer rings, which indicates the occurrence of moganite nanoparticles with the same crystal orientation.

low kinetic barrier can also be explained by the existence of structural and molecular water (*25*) available for incorporation in moganite (*13*, *16*). It is likely that sufficient water species generate a less-polymerized network, along with disruption of the larger ring in the crystal structure of moganite, as indicated in previous studies (*18*, *25*). Thus, these results demonstrate that the impact on NWA 2727 would have resulted in phase transitions from moganite to coesite and stishovite because of the low kinetic barriers of these transitions. In contrast, the moganite to stishovite transition took place only in the shock veins where shock pressure and temperature were significantly higher than in other regions. On the basis of the present analyses, moganite contents decrease and coesite and stishovite contents increase as the silica micrograins approached the shock veins (that is, regions with higher shock pressure and temperature during impact). However, these high-pressure SiO_2 phases are not derived from the remaining silica varieties such as fine-grained quartz in the basaltic clasts and coarse-grained tridymite and cristobalite (figs. S4 and S5). According to our findings, moganite in NWA 2727 would have been locally transformed into coesite and stishovite during the shock event on the Moon and therefore would have been a preexisting mineral before the impact.

In summary, our and previous findings provide positive evidence that moganite in NWA 2727 is most likely to be indigenous to the Moon, but the possibility that moganite is the result of terrestrial weathering is very low as described below.

1) Many previous publications on natural occurrences and laboratory experiments conclude that terrestrial moganite is restricted to formation by precipitating from alkaline fluid in a sedimentary setting under high-pressure consolidation at >100 MPa and >373 K. Meanwhile, moganite formation as a result of terrestrial weathering can be excluded because this scenario would imply a wide distribution of moganite in the sands of the hot desert where the meteorites were found, and this case has not been reported. Moganite is readily and completely lost via water alteration at ambient pressure.

2) Only NWA 2727 contains moganite, whereas its paired lunar meteorites of NWA 2977, 3333, and 6950 include neither moganite nor other silica polymorphs, despite the fact that all these NWA lunar meteorites fell to Earth at the same time and were discovered in the same location of the northwest African desert. Similarly, moganite is present in the breccia matrix of NWA 2727 but is seemingly absent in the gabbroic and basaltic clasts. If moganite is a terrestrial weathering product, then it should occur anywhere in these lunar meteorites, but that has not been observed.

3) Coesite and stishovite invariably coexist with moganite in the numerous silica micrograins ($n = 102$) of the breccia matrix of NWA 2727, but they do not occur together with quartz in the basaltic clasts and euhedral coarse-grained tridymite and cristobalite. As reported in previous studies, the coexisting low-pressure silica polymorphs within silica grains are considered to be a precursor of these high-pressure SiO_2 phases before the impact on the Moon. Moganite-rich domains are located inside the outer rims of coesite and stishovite in NWA 2727. This core-rim relationship is the opposite of what is observed in terrestrially weathered specimens, with a more strongly weathered rim containing little or no moganite and a pristine core rich in moganite, as reported in previous studies.

This important evidence supports the strong possibility that moganite in NWA 2727 formed during lunar alkaline fluid activity, rather than terrestrial weathering. However, robust evidence for lunar origin of moganite is still required; for instance, future sample return programs or in situ observations should search for moganite, particularly in rocks similar to the gabbro-basalt breccia of NWA 2727. Unfortunately, this observation cannot be confirmed using existing returned samples because a similar gabbro-basalt breccia lithology has not been found in the Apollo or Luna collections. Furthermore, it is essential to determine stability conditions of moganite in the low-pressure and low-temperature regions by hydrothermal experiments as well as the thermodynamic and kinetic calculations.

Impact event recorded in NWA 2727

Within almost all the silica micrograins, moganite-rich domains are enclosed by outer rims of coesite (Figs. 2 to 4 and fig. S3). In the case of terrestrial retrograde metamorphic rocks, relict coesite is invariably surrounded by a microcrystalline rim of chalcedony and quartz as a result of decompression (*26*). This presentation contrasts sharply with the coesite- and moganite-bearing silica micrograins in NWA 2727. Minor amounts of secondary quartz inclusions, which were back-transformed from high-pressure SiO_2 polymorphs because of a rapid decompression process during the shock event, are observed together with massive SiO_2 glass and coesite in the Asuka-881757 lunar meteorite (*10*). Silica micrograins, especially in the shock veins, should include minor amounts of moganite in the rim and abundant coesite in the core if this post-shock decompression would have led to the formation of moganite, but this is not the case. Moganite is abundant in the cores, and relatively abundant coesite coexists with small amounts of moganite (the left part in

Fig. 2C) and almost no moganite (the right part in Fig. 2C) in the rims of the silica micrograins in NWA 2727. This conclusion is strongly supported by the fact that moganite content increases with the distance of the silica micrograins from the shock veins (6 to 46 wt % with an average of 24 wt % in the shock veins, but 37 to 96 wt % with an average of 77 wt % in the breccia matrix far from these veins). Therefore, moganite is not considered to have been a back-transformation product generated during decompression. These observations indicate that coesite and stishovite would have been transformed from moganite via solid-state reactions when the shock reached peak pressure (during compression).

Continuous shock veins crosscut both the clasts and the breccia matrix of NWA 2727 (fig. S2), which implies their formation after brecciation, that is, the latest impact event when the meteorite was launched from the Moon. Our findings indicate that moganite transformed into coesite, stishovite, and cristobalite within each individual silica micrograin during this impact. On the basis of the pressure-temperature phase diagram for SiO_2 (*10*, *27*), the occurrence of stishovite sets constraints for peak pressures of at least 8 GPa below melting temperatures, that is, in the case of a solid-state reaction. Plagioclase transformed into maskelynite in the shock veins of NWA 2727, whereas it remains crystalline in the breccia matrix and clast regions far from the shock veins (fig. S6). This finding suggests that NWA 2727 experienced peak shock pressure below 22 GPa because Ca-rich plagioclase becomes completely amorphous above this pressure (*28*). On the basis of these considerations, the peak shock pressure recorded in NWA 2727 must have been in the pressure range of 8 to 22 GPa.

The Hugoniot data of CV chondrites (*29*) in this pressure range reveal similar chemical compositions and physical properties to those of NWA 2727, which provide constraints on its post-shock temperature of about 673 to 1073 K. Moganite undergoes phase transformation into cristobalite upon heating at temperatures higher than or equal to 1173 K (*13*), likely with a positive Clapeyron slope. Moganite is accompanied by cristobalite inside the silica micrograins only in the shock veins in NWA 2727 (fig. S3). Therefore, the post-shock temperature would be higher than 1173 K in the shock veins and about 673 to 1073 K in the other regions such as in the breccia matrix. Coesite would have been formed through solid-state transitions from moganite in the breccia matrix located far from the shock veins because its inferred post-shock temperature did not exceed the solidus temperature of bulk gabbroic composition (*27*). Furthermore, stishovite and coesite discovered in various meteorites are considered to have been transformed from low-pressure silica varieties by shock-induced compression at a temperature below the melting point (*10*, *23*). That is, these high-pressure SiO_2 phases in NWA 2727 are unlikely to be a product of the melt quenching process. From these results, we have estimated that NWA 2727 experienced a peak shock pressure of 8 to 22 GPa and post-shock temperatures of >1173 K in the shock veins and 673 to 1073 K in the other regions.

Although moganite is a thermochemically metastable phase (*6*, *7*, *13*), it can be preserved after a shock impact on the Moon for reasons described below. We performed shock recovery experiments on terrestrial moganite at 14.1 to 45.3 GPa (see Materials and Methods) and investigated the post-shock samples using micro-Raman spectroscopy. Moganite was detected in the shock-recovered samples at pressures below 25.0 GPa, whereas this phase was not detected at 34.2 to 45.3 GPa because of pressure-induced amorphization (fig. S10). In static experiments (*30*), moganite was partially vitrified at 25 to 30 GPa and completely vitrified above 40 GPa. At temperatures higher than 1173 K, the moganite-to-cristobalite phase transition takes place (*13*), likely with a positive Clapeyron slope. Thus, moganite in NWA 2727 undoubtedly remains after the shock impact at 8 to 22 GPa and 673 to 1073 K. Some of the moganite grains seem to have been converted to coesite, stishovite, shock-induced glass, and cristobalite, especially in the shock veins (>1173 K) and at the boundaries of the breccia matrix–hosted silica micrograins. Both of these locations underwent significantly higher impact-induced compaction with pressure and temperature compared with the other regions (*10*, *23*, *24*).

Formation of lunar moganite and H_2O ice in the subsurface

Abundant SiO_2 particles with an average radius of 4.5 nm are found as nanocrystalline aggregates in the moganite-bearing silica micrograins (Fig. 5). Similar SiO_2 nanoparticles (2 to 8 nm in radius) have been detected in Saturn's moon Enceladus by the Cassini Cosmic Dust Analyzer (*31*). According to theoretical and experimental models (*31*), silica particles grow from 1 to 1.5 to <10 nm in radius on time scales ranging from months to years when the alkaline solution at pH 7.5 to 10.5 and >363 K becomes supersaturated in SiO_2 within a serpentine-talc/saponite buffer system. The SiO_2 nanoparticles in the silica micrograins containing moganite also fulfill this condition. Moreover, this interpretation may be supported by a possible serpentine relict in other KREEP-like lunar meteorites (*32*). The relatively high-temperature regions within KREEP-like rocks are limited to the sunlit surface of the Procellarum KREEP Terrene (PKT) (*11*) [maximum temperatures of 390 to 399 K (*33*)]. Therefore, we interpret that the moganite-bearing silica micrograins originated from alkaline fluid activity on the sunlit surface within the PKT.

The source fluid of lunar moganite would have become cold-trapped as ice in the subsurface below its freezing point, similar to H_2O molecules in the uppermost thin regolith layers (*3*). In this sense, water ice has recently been detected by the Lunar Crater Observation and Sensing Satellite (LCROSS), dug out from subsurface regions deeper than about 0.7 m within the PSR near the South Pole Aitken (SPA) basin (*2*). Thus, this water ice is the most likely candidate for the source fluid of lunar moganite in the host gabbroic-basaltic brecciated bodies of NWA 2727 in the PKT and SPA subsurfaces. On the basis of a comparison of our results with previously reported data, a formation process for lunar moganite can be explained in chronological order as follows (Fig. 6).

According to the $^{147}Sm/^{143}Nd$ age (*12*) and petrological features (*11*) of the NWA 773 clan (including NWA 2727), a host rock of the OC gabbroic clasts crystallized in a shallow intrusive chamber within the lunar crust, whereas basaltic clasts solidified via magmatic eruption at the surface of the PKT at 2.993 ± 0.032 billion years (Ga) ago.

i) Subsequent impact events occurred on the surface at <2.67 ± 0.04 Ga ago (*11*, *34*), because this ^{40}Ar-^{39}Ar step-heating age is sensitive to the post-shock temperature (*10*, *23*) and does not indicate complete reset, although it is younger than the other radio-isotope ages (*11*, *12*, *34*). According to recent modeling (*35*), carbonaceous chondrite collisions, rather than comets, are the most significant contributors (>80%) to the presence of water in the early Moon. Most carbonaceous chondrites contain large amounts of water species and hydrous products (for example, serpentine) that originated from alkaline fluids within a pH range of 7.0 to 12.0 in the parent bodies (*36*). These conditions are in good agreement with the pH range of 9.5 to 10.5 and temperature range of 363 to 399 K of the fluid activities that precipitate both moganite (*17*) and SiO_2 nanoparticles with radii <10 nm (*31*) on the sunlit surface (*33*). This finding implies that this alkaline water would have been delivered to the PKT via carbonaceous chondrite collisions.

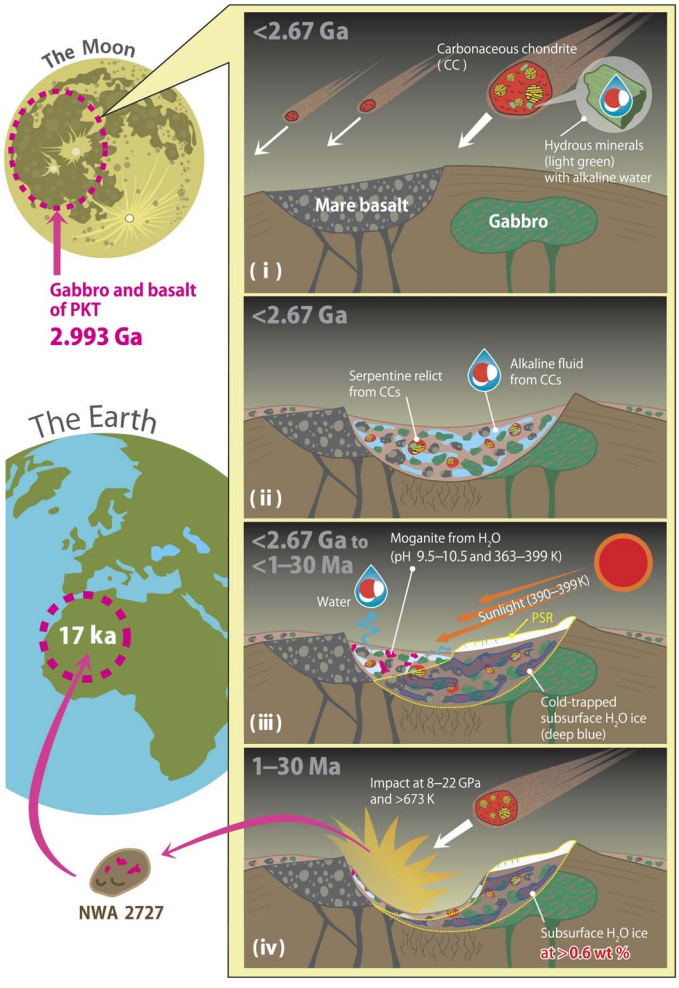

Fig. 6. Chronological schematic of the history of subsurface H_2O in the Moon and the formation of moganite. This history can be drawn in chronological order, based on the present study and previous works. At 2.993 ± 0.032 Ga, mare basalt (gray) solidified on the lunar surface, and a gabbroic intrusive chamber (green) crystallized in the anorthositic crust (brown) of the PKT. (i) Carbonaceous chondrite (CC) collisions are considered to have occurred at <2.67 ± 0.04 Ga, which led to the delivery of alkaline water to the PKT. (ii) After these collisions, constituent rocks of the PKT and carbonaceous chondrite fragments (that is, a serpentine relict) would have been ejected and brecciated in the impact basin. During breccia consolidation, water delivered by the carbonaceous chondrites was captured as fluid inside the breccia. (iii) On the sunlit surface at 363 to 399 K, the captured H_2O (pH 9.5 to 10.5) is likely to have become a silicic acid fluid and have migrated to space and the colder regions. Then, it would have precipitated moganite nanoparticles under high consolidation pressure after (ii) the first collisions at <2.67 ± 0.04 Ga and before (iv) the most recent impact at 1 to 30 Ma as expressed below, or perhaps at <130 Ma. Below its freezing point, it would have been simultaneously cold-trapped in the subsurface down to the depth of the impact basin and PSR. (iv) A subsequent heavy impact event at 1 to 30 Ma may have been launched NWA 2727 from the Moon, which resulted in partial phase transitions from moganite to coesite, stishovite, and cristobalite. The estimated size of impactor that collided on the Moon in this period is at least ~0.1 km in diameter, which formed an impact crater with a diameter of at least ~1 km, based on the shock pressure, temperature, and grain size of stishovite obtained by the present study and a calculation procedure reported in a previous study (*23*). NWA 2727 eventually may have fallen to Earth at 17 ± 1 thousand years (ka) ago. A subsurface H_2O concentration higher than the estimated bulk content of 0.6 wt % is expected to still remain as ice.

ii) After these collisions, ejecta of anorthositic crust, mare basalt, and gabbroic intrusive bodies were consolidated and brecciated on the surface of the impact basin (*11*). A possible serpentine relict in KREEP-like lunar meteorites (*32*) may support the hypothesis of collisions and subsequent incorporations of carbonaceous chondrite fragments into the brecciated bodies within the PKT. It is highly likely that the alkaline water delivered by these collisions was captured as a fluid inside the breccia via consolidation.

iii) Below the freezing point, this captured fluid would have been cold-trapped as H_2O ice in the subsurface of the gabbroic-basaltic brecciated bodies at depths ranging from 10^{-4} to $>10^2$ m [a thermal stable region of H_2O ice (*3*)] or down to the bottom of the basin, where it would remain for billions of years, according to its calculated residence time (*3*). Simultaneously, at 363 to 399 K on the sunlit surface, the moganite-bearing silica micrograins would have been precipitated from the captured H_2O fluids at pH 9.5 to 10.5 in the interstices of the breccia matrix–hosted constituent minerals. These grains formed after (ii) the first collisions at <2.67 ± 0.04 Ga and before (iv) the most recent impact at >1 to 30 Ma as explained below, or perhaps at <130 Ma based on the absence of metastable moganite in sedimentary rocks older than this age (*13*, *15*, *16*). The SiO_2 nanoparticles continued to grow to radii of 4.5 nm for months to years on average. After precipitation, a fraction of the captured H_2O fluids was released into space, whereas the remaining fraction migrated vertically downward and horizontally toward colder regions to be subsequently added to the H_2O ice in the subsurface underneath the PSR via a H_2O migration model (*3*). Similarly, the delivered and then captured H_2O may have accumulated as ice in the SPA subsurface, as observed by LCROSS (*2*).

iv) The NWA 773 clan was launched from the surface of the gabbroic-basaltic brecciated bodies within the PKT by the most recent impact event at 8 to 22 GPa and >673 K, which led to transformations of some of the moganite to coesite, stishovite, and cristobalite phases. This shock metamorphism possibly occurred at about 1 to 30 Ma, as indicated by the transition time of NWA 773 (*22*). Finally, the NWA 773 clan may have fallen to Earth at a terrestrial age of 17 ± 1 ka (*22*).

Bulk content of subsurface H_2O ice calculated from moganite solubility

The bulk content of this subsurface H_2O ice in the PKT and SPA can be theoretically calculated on the basis of the petrological features of NWA 2727, the formation process of moganite, and the silica precipitation model. By combining electron microscopic observations with a digital image analysis, modal compositions of NWA 2727 by weight percentage were determined to be 35.6, 5.3, and 59.1 wt % for the OC gabbroic clasts, basaltic clasts, and breccia matrix, respectively (see Materials and Methods). Furthermore, on the basis of these modal compositions, the bulk content of moganite-bearing silica reaches 76 ppm by weight. Assuming an equilibrium reaction of SiO_2 (*s*) + $2H_2O \leftrightarrow H_4SiO_4$ (*aq*), the amount of water reacting with 76 ppm of a solid moganite could be calculated from the moganite solubility in water at varying pH values and temperatures.

According to hydrothermal experiments (*14*), the moganite solubilities obtained from the equilibrium constants for this reaction and the molality of moganite in water (*14*) are 44 and 163 mg/kg of silica upon reaction with water at a pH of 3.5 at temperatures of 298 and 373 K, respectively. However, values for pH 9.5 to 10.5 and 363 to 399 K, which, as revealed by our findings, correspond to the conditions of moganite precipitation on the Moon, are lacking. Reliable data of the equilibrium reaction of various SiO_2 polymorphs (for example, quartz and amorphous

silica) with H_2O into aqueous silicic acid have been previously reported (*37*). This model is temperature-dependent and can be expressed by the following equation

$$\log C = -848/T + 4.47 \quad (1)$$

where C is the moganite concentration in milligram per kilogram and T is the absolute temperature in kelvin. We also set up simultaneous equations of $C_1 = 44$ mg/kg for $T_1 = 298$ K and $C_2 = 163$ mg/kg for $T_2 = 373$ K to evaluate the temperature-independent coefficients (−848 and 4.47 for moganite). This equation is valid for 273 to 523 K (*37*) and pH 3.5 (*14*).

In addition, the solubility of various SiO_2 polymorphs (S) as a function of pH can be derived as follows (*37*)

$$S = C[1 + \{10^{pH} \times K_1/\gamma(H_3SiO_4^-)\}] \quad (2)$$

$$\log K_1 = -2549/T - 15.36 \times 10^{-6} T^2 \quad (3)$$

where K_1 is the dissociation constant for this reaction and γ ($H_3SiO_4^-$) is the activity coefficient of $H_3SiO_4^-$ that can be calculated from the extended Debye-Huckel equation and the ionic strength of the solution (*37*). Because Eqs. 2 and 3 have been used to calculate the pH-dependent solubilities of both crystalline and amorphous silica, they would be applicable to moganite. The solubility of moganite ranged from 0.62 g/kg of silica (pH 9.5 and T = 363 K) to 13.0 g/kg of silica (pH 10.5 and T = 399 K). Although silica solubility in water tends to increase with pressure (*38*), the effect is negligible when the temperature is relatively low, as in this case. On the basis of these moganite solubilities at pH 9.5 to 10.5 and 363 to 399 K, a bulk H_2O content of at least 0.6 to 12.3 wt % is necessary to precipitate 76 ppm of a solid moganite from the silicic acid fluid. Accordingly, H_2O molecules would be cold-trapped as ice at the estimated bulk contents of >0.6 wt % in the subsurface of the host gabbroic-basaltic bodies below their freezing point.

The estimated bulk content (>0.6 wt %) of H_2O ice in the Moon's subsurface calculated here is in excellent agreement with the concentrations of H_2O ice (5.6 ± 2.9% by mass) excavated from the SPA subsurface by LCROSS (*2*), OH and H_2O molecules (~0.3 wt %) on the North Pole observed by Deep Impact (*1*), and water-equivalent hydrogen (~0.5 wt %) on various craters of the SPA found by Lunar Prospector (*4*). Furthermore, this value is significantly higher than the bulk contents of structural OH species found in lunar crustal rocks, such as basalt and anorthosite (<1 parts per billion to 6.4 ppm) (*39*), as well as that of solar wind–induced hydroxyl groups (about 70 ppm) in the surface regolith (*39*), which is thought to represent the most water-enriched rocks on the Moon. In the subsurface of the host rock bodies of NWA 2727 within the PKT and SPA regions, H_2O molecules would have become cold-trapped simultaneously with the formation of moganite perhaps at <130 Ma or at least 2.67 ± 0.04 Ga (Fig. 6). This subsurface H_2O is expected to still remain as ice today because it can theoretically and observationally survive over billions of years (*2*, *3*). In the impact craters within the PKT and SPA regions, the spacecraft SELENE discovered local sites of olivine- and ejected pyroxene–dominated exposures (*40*). These plutonic sites are one of the candidates that have abundant H_2O ice remaining in the subsurface because they have similar chemical compositions to NWA 2727. Subsurface H_2O ice can be extracted from exposed rocks more easily than hydroxyl groups from crustal rocks and regolith soils because the hydroxyl group is strongly linked with the structure of minerals and is dehydrated by heating at quite high temperatures. Therefore, moganite is a valuable marker of these abundant and available subsurface water resources for human exploration on the Moon. In addition, we emphasize that further discovery of moganite in material from new sample return programs may be important because of the absence of these gabbroic-basaltic brecciated rocks in the existing Apollo and Luna samples.

MATERIALS AND METHODS

Lithologies of lunar meteorites

Lunar meteorites of gabbroic-basaltic breccia (NWA 2727), nonbrecciated gabbro (NWA 2977, 3333, and 6950), anorthositic regolith breccia (NWA 5000, 6355, 8668, and 10649 and Dar al Gani 400), nonbrecciated basalt (NWA 032 and 4734), and nonbrecciated troctolite (NWA 5744 and 8599) were examined here by microanalysis, but moganite was found only in NWA 2727. Among these samples, NWA 2727 is paired with NWA 2977, 3333, and 6950, all of which are classified in the NWA 773 clan and are typically composed of an OC gabbroic lithology. Exceptionally, NWA 2727 contains this OC gabbro and pyroxene phyric basalt lithic clasts within its breccia matrix (*11*, *12*). The NWA 773 clan is characterized by KREEP-like compositions with very low Ti, with the same crystallization (2.993 ± 0.032 Ga), shock metamorphic (<2.67 ± 0.04 Ga), transition (1 to 30 Ma), and terrestrial ages (17 ± 1 ka) (*11*, *12*, *22*, *34*). The OC gabbroic clasts are thought to have differentiated in the shallow intrusive chamber of the crust within the PKT via assimilation with the KREEP-rich layer in the mantle, and the basaltic clasts are thought to have solidified after magmatic eruptions of this assimilated melt on the PKT surface (*11*).

False-color elemental mapping of Mg (red), Fe (green), and Al (blue) Kα x-rays was performed to distinguish the lithologies of NWA 2727 based on the modal and chemical compositions of the constituent minerals (Fig. 1). NWA 2727 mainly consists of Mg/Fe-rich OC gabbroic and clinopyroxene phyric basaltic clasts (areas enclosed by the solid and dashed white lines, respectively, in Fig. 1) contained in a breccia matrix (other areas). The OC gabbroic clasts contain constituent minerals of euhedral olivine (orange and yellow grains in Fig. 1) and clinopyroxene (brown and green grains) as single crystals (0.1 to 0.5 mm in radius), with minor amounts of anhedral plagioclase (blue grains) between the olivine and clinopyroxene crystals. The basaltic clasts contain clinopyroxene phenocrysts within a groundmass of clinopyroxene, plagioclase with small fine-grained quartz crystals (10 to 20 μm in radius; n = 23) (Fig. 1 and fig. S4B). Numerous fine to coarse lithic grains (<50 μm in radius) of OC gabbro and basalt with small amygdaloidal silica micrograins (2 to 13 μm in radius; n = 102 for the breccia matrix far from the shock veins and n = 4 for those entrained in the shock veins) containing moganite fill the interstices between these clasts as a breccia matrix (Fig. 1 and fig. S1). These silica micrograins are surrounded by pervasive radiating cracks similar to those previously reported in silica from shocked meteorites (*23*). Coarse grains of euhedral tridymite and cristobalite (20 to 100 μm in radius; n = 35) are also present in NWA 2727 (fig. S4A) and are gathered as felsic lithologies.

The average volume ratios of each lithology (35.5, 5.4, and 59.1 volume % for the OC gabbroic clasts, basaltic clasts, and breccia matrix, respectively) for the NWA 2727 samples were determined using electron microscopy. The breccia matrix can be roughly divided into two types of breccia based on the volume ratios of these clasts [that is, OC gabbroic (51.4 volume %) and basaltic (7.7 volume %) breccia]. According to the modal compositions and densities of olivine, pyroxene, and plagioclase in these

lithologies, the volume ratios can be converted into weight percentages for each constituent mineral (35.6, 5.3, and 59.1 wt % for the OC gabbroic clasts, basaltic clasts, and breccia matrix, respectively).

We also identified continuous shock veins (<5 mm in length and about 200 μm in width) in the backscattered electron (BSE) images defined by fine mineral fragments and impact melt glasses with bubble marks and flow textures (fig. S2). The continuous shock veins crosscut both the clasts and the breccia matrix. This finding reveals that the formation of shock veins occurred after brecciation. Accordingly, the latest impact event that launched NWA 2727 from the Moon to Earth would have generated the shock veins.

Microanalyses

We prepared three polished thin sections of different fragments of NWA 2727, with and without continuous shock veins through both the clasts and the breccia matrix, for various microanalyses. A false-color x-ray elemental mapping of the carbon-coated NWA 2727 thin sections was performed using a wavelength-dispersive x-ray spectrometer attached to the EPMA (JXA-8900, JEOL) at Kobe University. The obtained elemental maps of Mg, Fe, and Al Kα x-rays were combined with an image processing software (that is, ImageJ; http://rsbweb.nih.gov/ij/) to analyze the modal and chemical compositions of olivine, pyroxene, and plagioclase within the NWA 2727 samples. BSE images of the minerals in NWA 2727 were obtained using an SEM (JSM-5800, JEOL) equipped with an energy-dispersive x-ray spectrometer (EDS) at Kobe University. The focused electron beam was set at 15 keV and 20 nA with a step size of 10 μm for EPMA and 15 keV and 0.4 nA for SEM analyses. On the basis of the BSE images of NWA 2727, the grain radii of the moganite-bearing silica grains (n = 102) were evaluated using the Analyze Particles tool of the ImageJ software, where they were converted from each area of the grains assuming a perfectly spherical shape.

Raman spectroscopy was performed on the NWA 2727 samples using a laser micro-Raman spectrometer (Nicolet Almega XR, Thermo Electron) at the Laboratory of Infra-Red and Raman Spectroscopy at Thermo Fisher Scientific K.K. Laser power (Nd:YAG, 532-nm excitation line) was fixed at 20 mW on the sample with a spot size of about 2 μm. The Raman spectra for each mineral are within the range of 100 to 800 cm^{-1} with a step width of 1 cm^{-1}. These spectra were collected in 10 accumulations of 60-s exposure times for one-by-one analysis and five accumulations of 10-s exposure times for Raman mapping. All spectral data were calibrated by monitoring the position of the O–Si–O bending vibration with regard to that of silica polymorphs (high–optical grade standard quartz, high-purity terrestrial moganite and cristobalite, and synthetic coesite and stishovite) before and after each measurement, which ensures an analytical reproducibility of less than 1 cm^{-1}. Raman mapping was measured over 17 × 23–μm to 23 × 40–μm areas in steps of 1 μm. The Raman spectra of each analytical point in the mapping were deconvolved on the basis of Lorentzian curve fitting, and the calculated integral intensities of the main bands were subsequently used to obtain the Raman intensity maps of each silica polymorph. The moganite content of the silica grains (that is, the weight percentage of moganite versus other polymorphs such as quartz, coesite, and amorphous SiO_2 glass) in NWA 2727 was also determined using Raman spectroscopy. The Raman spectral data of the silica micrograins (n = 102) were fitted with Lorentzian functions to acquire the integral band intensities of each SiO_2 polymorph, and their intensity ratios were converted into moganite contents using the calibration curve (*8*, *9*).

Several silica grains in NWA 2727 were excavated with the FIB system (Quanta 200 3DS, FEI) at Kyoto University. Specific square cube (about 10 μm side) portions were extracted by a gallium ion beam at 5 to 30 kV and 0.01 to 30 nA and subsequently fixed to a micrometer-sized copper mesh pillar through platinum deposition for SR-XRD and TEM analyses. A monochromatic incident x-ray beam at SPring-8 BL10XU with a wavelength of 0.41569(9) Å was focused to <10 μm in diameter. The angle-dispersive XRD data were collected with an imaging plate using an exposure time of 5 min and analyzed with the PDIndexer, IPAnalyzer, and CSManager software (http://pmsl.planet.sci.kobe-u.ac.jp/~seto/). We also acquired angle-dispersive XRD data for cerium dioxide (CeO_2) to calibrate both the wavelength and the distance between the samples and the imaging plate.

The cubic samples were thinned into <100 nm in thickness by the gallium ion beam attached to the FIB system for TEM (JEM-2100F, JEOL; accelerating voltage, 200 kV) observation at Kobe University. Annular dark-field STEM images were captured, and false-color combined elemental maps of Si, Mg, and Al Kα x-rays were recorded for the processed thin-foil samples on the STEM-EDS system. We also performed high-magnification bright-field TEM of SiO_2 regions in the false-color maps of the processed thin-foil samples. The ImageJ software was used to analyze the grain radii of the SiO_2 nanoparticles (n = 148) observed in the bright-field TEM images. Grain radii below 1 nm were not considered because they could not be distinguished from noise. The crystal structure of the SiO_2 nanoparticles was identified on the basis of SAED (spot size, 60 nm in radius), the patterns of which were analyzed using the ImageJ and ReciPro software (http://pmsl.planet.sci.kobe-u.ac.jp/~seto/). Specific areas of these SiO_2 nanoparticles with relatively large sizes were examined via SAED analyses while varying the direction of the zone axis.

SEM-CL spectroscopy was carried out to determine the CL spectra from 300 to 800 nm in 1-nm steps using SEM (JSM-5410, JEOL) combined with a grating monochromator (Mono CL2, Oxford) at the Okayama University of Science. The CL signal was recorded by a photon counting method using a photomultiplier tube (R2228, Hamamatsu). All CL spectra were measured at 15 kV and 2.0 nA, and the obtained spectral data were corrected for total instrumental response and determined using a calibrated standard lamp to quantify the intensity and the wavelength.

Shock recovery experiments

Nearly pure moganite microcrystals with a content of 85 to 100 wt % from Gran Canaria were selected as the starting material for shock recovery experiments. Powder samples (porosities of 12 to 27%) were enclosed in SUS304 stainless steel containers (30-mm diameter × 30-mm length). The samples (about 1 mm in thickness) were set 3 mm in depth from the impact surface. A propellant gun with a 30-mm bore (National Institute for Materials Science) was used to accelerate a projectile with a metal flyer plate (29-mm diameter × 3-mm thickness; Al alloy for the 14.1-GPa shot and SUS304 for the other shots) to the required velocity. Considering the large thickness ratio of the flyer to the samples, the shock pressure generated in the sample is inferred to reach an equilibrium with that of the container. On the basis of this approximation, the peak shock pressure was determined using the impedance matching method using the measured impact velocity of the projectile and the shock compression curve (Hugoniot) of the stainless steel container. The measured flyer velocity and the calculated equivalent peak shock pressure are 1.145 km/s and 14.1 GPa, 1.043 km/s and 22.0 GPa, 1.165 km/s and 25.0 GPa, 1.462 km/s and 34.2 GPa, and 1.517 km/s and 45.3 GPa. The recovered samples, as well as the moganite starting material, were embedded on a slide glass with epoxy resin, polished, and mirror-finished with 1-μm diamond abrasive before Raman spectroscopy measurements.

SUPPLEMENTARY MATERIALS

Supplementary material for this article is available at http://advances.sciencemag.org/cgi/content/full/4/5/eaar4378/DC1

fig. S1. BSE images of silica in the breccia matrix and the shock veins of NWA 2727.
fig. S2. BSE image of the shock vein of NWA 2727.
fig. S3. Micro-Raman analyses of high-pressure and high-temperature SiO_2 phases.
fig. S4. BSE images of silica varieties in various lithologies of NWA 2727.
fig. S5. Single crystals of anhedral quartz in a basaltic clast.
fig. S6. Spectroscopic identification of maskelynite and plagioclase.
fig. S7. SR-XRD analyses of various SiO_2 phases.
fig. S8. TEM chemical composition analyses.
fig. S9. TEM observations of coesite, stishovite, and cristobalite.
fig. S10. Micro-Raman spectroscopy of unshocked and experimentally shock-recovered moganite.

REFERENCES AND NOTES

1. J. M. Sunshine, T. L. Farnham, L. M. Feaga, O. Groussin, F. Merlin, R. E. Milliken, M. F. A'Hearn, Temporal and spatial variability of lunar hydration as observed by the deep impact spacecraft. *Science* **326**, 565–568 (2009).
2. A. Colaprete, P. Schultz, J. Heldmann, D. Wooden, M. Shirley, K. Ennico, B. Hermalyn, W. Marshall, A. Ricco, R. C. Elphic, D. Goldstein, D. Summy, G. D. Bart, E. Asphaug, D. Korycansky, D. Landis, L. Sollitt, Detection of water in the LCROSS ejecta plume. *Science* **330**, 463–468 (2010).
3. N. Schorghofer, G. J. Taylor, Subsurface migration of H_2O at lunar cold traps. *J. Geophys. Res.* **112**, E02010 (2007).
4. A. B. Sanin, I. G. Mitrofanov, M. L. Litvak, B. N. Bakhtin, J. G. Bodnarik, W. V. Boynton, G. Chin, L. G. Evans, K. Harshman, F. Fedosov, D. V. Golovin, A. S. Kozyrev, T. A. Livengood, A. V. Malakhov, T. P. McClanahan, M. I. Mokrousov, R. D. Starr, R. Z. Sagdeev, A. A. Vostrukhin, Hydrogen distribution in the lunar polar regions. *Icarus* **283**, 20–30 (2017).
5. S. Li, R. E. Milliken, P. G. Lucey, E. Fisher, Possible detection of surface water ice in the lunar polar regions using data from the Moon Mineralogy Mapper (M^3), in *Proceedings of the 48th Lunar and Planetary Science Conference*, The Woodlands, TX, 20 to 24 March 2017.
6. P. J. Heaney, J. E. Post, The widespread distribution of a novel silica polymorph in microcrystalline quartz varieties. *Science* **255**, 441–443 (1992).
7. P. J. Heaney, Moganite as an indicator for vanished evaporites: A testament reborn? *J. Sediment. Res.* **65**, 633–638 (1995).
8. J. Götze, L. Nasdala, R. Kleeberg, M. Wenzel, Occurrence and distribution of "moganite" in agate/chalcedony: A combined micro-Raman, Rietveld, and cathodoluminescence study. *Contrib. Mineral. Petrol.* **133**, 96–105 (1998).
9. P. Schmidt, L. Bellot-Gurlet, V. Lèa, P. Sciau, Moganite detection in silica rocks using Raman and infrared spectroscopy. *Eur. J. Mineral.* **25**, 797–805 (2013).
10. E. Ohtani, S. Ozawa, M. Miyahara, Y. Ito, T. Mikouchi, M. Kimura, T. Arai, K. Sato, K. Hiraga, Coesite and stishovite in a shocked lunar meteorite, Asuka-881757, and impact events in lunar surface. *Proc. Natl. Acad. Sci. U.S.A.* **108**, 463–466 (2011).
11. B. L. Jolliff, R. L. Korotev, R. A. Zeigler, C. Floss, Northwest Africa 773: Lunar mare breccia with a shallow-formed olivine-cumulate component, inferred very-low-Ti (VLT) heritage, and a KREEP connection. *Geochim. Cosmochim. Acta* **67**, 4857–4879 (2003).
12. L. E. Borg, A. M. Gaffney, C. K. Shearer, D. J. DePaolo, I. D. Hutcheon, T. L. Owens, E. Ramon, G. Brennecka, Mechanisms for incompatible-element enrichment on the Moon deduced from the lunar basaltic meteorite Northwest Africa 032. *Geochim. Cosmochim. Acta* **73**, 3963–3980 (2009).
13. I. Petrovic, P. J. Heaney, A. Navrotsky, Thermochemistry of the new silica polymorph moganite. *Phys. Chem. Miner.* **23**, 119–126 (1996).
14. S. R. Gíslason, P. J. Heaney, E. H. Oelkers, J. Schott, Kinetic and thermodynamic properties of moganite, novel silica polymorph. *Geochim. Cosmochim. Acta* **61**, 1193–1204 (1997).
15. G. Parthasarathy, A. C. Kunwar, R. Srinivasan, Occurrence of moganite-rich chalcedony in Deccan flood basalts, Killari, Maharashtra, India. *Eur. J. Mineral.* **13**, 127–134 (2001).
16. T. Moxon, S. Ríos, Moganite and water content as a function of age in agate: An XRD and thermogravimetric study. *Eur. J. Mineral.* **16**, 269–278 (2004).
17. O. Schäf, H. Ghobarkar, A. Garnier, C. Vagner, J. K. N. Lindner, J. Hanss, A. Reller, Synthesis of nanocrystalline low temperature silica polymorphs. *Solid State Sci.* **8**, 625–633 (2006).
18. A. Kyono, M. Yokooji, T. Chiba, T. Tamura, A. Tuji, Pressure–induced crystallization of biogenic hydrous amorphous silica. *J. Mineral. Petrol. Sci.* **112**, 324–335 (2017).
19. V. V. Murashov, I. M. Svishchev, Quartz family of silica polymorphs: Comparative simulation study of quartz, moganite, and orthorhombic silica, and their phase transformations. *Phys. Rev. B. Condens. Matter* **57**, 5639–5646 (1998).
20. M. R. Lee, P. A. Bland, Mechanisms of weathering of meteorites recovered from hot and cold deserts and the formation of phyllosilicates. *Geochim. Cosmochim. Acta* **68**, 893–916 (2004).
21. R. L. Korotev, Lunar meteorites from Oman. *Meteorit. Planet. Sci.* **47**, 1365–1402 (2012).
22. K. Nishiizumi, D. J. Hillegonds, L. R. McHargue, A. J. T. Jull, Exposure and terrestrial histories of new lunar and martian meteorites, in *Proceedings of the 35th Lunar and Planetary Science Conference*, The Woodlands, TX, 15 to 19 March 2004.
23. M. Miyahara, S. Kaneko, E. Ohtani, T. Sakai, T. Nagase, M. Kayama, H. Nishido, N. Hirao, Discovery of seifertite in a shocked lunar meteorite. *Nat. Commun.* **4**, 1737 (2013).
24. P. A. Bland, G. S. Collins, T. M. Davison, N. M. Abreu, F. J. Ciesla, A. R. Muxworthy, J. Moore, Pressure–temperature evolution of primordial solar system solids during impact-induced compaction. *Nat. Commun.* **5**, 5451 (2014).
25. A. Arasuna, M. Okuno, T. Mizukami, M. Akaogi, T. Yokoyama, H. Okudera, S. Arai, The role of water in coesite crystallization from silica gel. *Eur. J. Mineral.* **25**, 791–796 (2013).
26. J. L. Mosenfelder, H.-P. Schertl, J. R. Smyth, J. G. Liou, Factors in the preservation of coesite: The importance of fluid infiltration. *Am. Mineral.* **90**, 779–789 (2005).
27. D. C. Presnall, Phase diagrams of Earth-forming minerals, in *Mineral Physics & Crystallography: A Handbook of Physical Constants*, T. J. Ahrens, Eds. (American Geophysical Union, 1995), pp. 248–268.
28. T. Kubo, M. Kimura, T. Kato, M. Nishi, A. Tominaga, T. Kikegawa, K.-i. Funakoshi, Plagioclase breakdown as an indicator for shock conditions of meteorites. *Nat. Geosci.* **3**, 41–45 (2010).
29. T. Nakamura, K. Tomeoka, N. Takaoka, T. Sekine, H. Takeda, Impact-induced textural changes of CV carbonaceous chondrites: Experimental reproduction. *Icarus* **146**, 289–300 (2000).
30. J.-M. Léger, J. Haines, C. Chateau, The high-pressure behaviour of the "moganite" polymorph of SiO_2. *Eur. J. Mineral.* **13**, 351–359 (2001).
31. H.-W. Hsu, F. Postberg, Y. Sekine, T. Shibuya, S. Kempf, M. Horányi, A. Juhász, N. Altobelli, K. Suzuki, Y. Masaki, T. Kuwatani, S. Tachibana, S.-i. Sirono, G. Moragas-Klostermeyer, R. Srama, Ongoing hydrothermal activities within Enceladus. *Nature* **519**, 207–210 (2015).
32. S. I. Demidova, M. A. Nazarov, T. Ntaflos, F. Brandstätter, Possible serpentine relicts in lunar meteorites. *Petrology* **23**, 116–126 (2015).
33. A. R. Vasavada, J. L. Bandfield, B. T. Greenhagen, P. O. Hayne, M. A. Siegler, J.-P. Williams, D. A. Paige, Lunar equatorial surface temperatures and regolith properties from the diviner lunar radiometer experiment. *J. Geophys. Res.* **117**, E00H18 (2012).
34. V. A. Fernandes, R. Burgess, G. Turner, ^{40}Ar-^{39}Ar chronology of lunar meteorites Northwest Africa 032 and 773. *Meteorit. Planet. Sci.* **38**, 555–564 (2003).
35. J. J. Barnes, D. A. Kring, R. Tartése, I. A. Franchi, M. Anand, S. S. Russell, An asteroidal origin for water in the Moon. *Nat. Commun.* **7**, 11684 (2016).
36. A. J. Brearley, The action of water, in *Meteorites and the Early Solar System II*, D. S. Lauretta, H. Y. McSween Jr., Eds. (University of Arizona Press, 2006), pp. 587–624.
37. K. Brown, Thermodynamics and kinetics of silica scaling, in *Proceedings of International Workshop on Mineral Scaling 2011*, Manila, Philippines, 25 to 27 May 2011.
38. P. Karásek, L. Šťavíková, J. Planeta, B. Hohnová, M. Roth, Solubility of fused silica in sub- and supercritical water: Estimation from a thermodynamic model. *J. Supercrit. Fluids* **83**, 72–77 (2013).
39. M. Anand, R. Tartése, J. J. Barnes, Understanding the origin and evolution of water in the Moon through lunar sample studies. *Philos. Trans. R. Soc. A Math. Phys. Eng. Sci.* **372**, 20130254 (2014).
40. S. Yamamoto, R. Nakamura, T. Matsunaga, Y. Ogawa, Y. Ishihara, T. Morota, N. Hirata, M. Ohtake, T. Hiroi, Y. Yokota, J. Haruyama, Possible mantle origin of olivine around lunar impact basins detected by SELENE. *Nat. Geosci.* **3**, 533–536 (2010).

Acknowledgments: We would like to thank T. Okuchi and N. Purevjav (Institute for Planetary Materials, Okayama University) for their critical discussions of the manuscript. We are indebted to R. Harui (Thermo Fisher Scientific K.K.) for conducting Raman spectroscopy, and H. Nishido and K. Ninagawa (Okayama University of Science) for guidance with CL spectroscopy. We are grateful to N. Kayama for proofreading this manuscript. Figure 6 was illustrated by M. Sasaoka (SASAMI-GEO-SCIENCE) (http://sasami7793.wixsite.com/sasami-geo-science). The SR-XRD measurements at SPring-8 BL10XU were performed under the proposal 2014B0104. **Funding:** This work was supported by Japan Society for the Promotion of Science KAKENHI grant number 26•4437 to M.K. and by Grant-in-Aid awards for Scientific Research number 15H05748 to E.O. **Author contributions:** M.K. outlined the study, performed all the analyses, and collected the samples. N.T., E.O., and Y.S. assisted with Raman spectroscopy, electron microscopy, and SR-XRD analyses and advised about the presence of water in the lunar subsurface. H.N. provided commentary on the mineralogy and petrology of lunar meteorites. J.G. advised about moganite. A.M. contributed to the setup and assisted with the FIB system. S.O., T.S., and M. Miyahara advised concerning shock metamorphism on the Moon. K.T., M. Matsumoto, and N.S. supported the SEM, EPMA, and TEM analyses. N.H. contributed in setting up the SR-XRD. T.S. and T.K. designed the shock recovery experiments. All authors participated in discussing the results and writing the manuscript. **Competing interests:** The authors declare that they have no competing interests. **Data and materials availability:** All data needed to evaluate the conclusions in this paper are presented in the paper and/or the Supplementary Materials. Additional data related to this paper may be requested from the authors.

Submitted 8 November 2017
Accepted 16 March 2018
Published 2 May 2018
10.1126/sciadv.aar4378

Citation: M. Kayama, N. Tomioka, E. Ohtani, Y. Seto, H. Nagaoka, J. Götze, A. Miyake, S. Ozawa, T. Sekine, M. Miyahara, K. Tomeoka, M. Matsumoto, N. Shoda, N. Hirao, T. Kobayashi, Discovery of moganite in a lunar meteorite as a trace of H_2O ice in the Moon's regolith. *Sci. Adv.* **4**, eaar4378 (2018).

Science Advances

Discovery of moganite in a lunar meteorite as a trace of H_2O ice in the Moon's regolith

Masahiro Kayama, Naotaka Tomioka, Eiji Ohtani, Yusuke Seto, Hiroshi Nagaoka, Jens Götze, Akira Miyake, Shin Ozawa, Toshimori Sekine, Masaaki Miyahara, Kazushige Tomeoka, Megumi Matsumoto, Naoki Shoda, Naohisa Hirao and Takamichi Kobayashi

Sci Adv **4** (5), eaar4378.
DOI: 10.1126/sciadv.aar4378